

Differentiated design strategies toward broadband achromatic and polarization-insensitive metalenses

Ximin Tian,^a Yafeng Huang,^a Junwei Xu,^{a,*} Tao Jiang,^b Pei Ding,^a Yaning Xu,^a Shenglan Zhang,^a and Zhi-Yuan Li^{c,*}

^aZhengzhou University of Aeronautics, School of Materials Science and Engineering, Zhengzhou, China

^bNanjing University, College of Engineering and Applied Sciences, National Laboratory of Solid State Microstructures, Nanjing, China

^cSouth China University of Technology, College of Physics and Optoelectronics, Guangzhou, China

Abstract. Metasurfaces have emerged as a flexible platform for shaping the electromagnetic field via the tailoring phase, amplitude, and polarization at will. However, the chromatic aberration inherited from building blocks' diffractive nature plagues them when used in many practical applications. Current solutions for eliminating chromatic aberration usually rely on searching through many meta-atoms to seek designs that satisfy both phase and phase dispersion preconditions, inevitably leading to intensive design efforts. Moreover, most schemes are commonly valid for incidence with a specific spin state. Here, inspired by the Rayleigh criterion for spot resolution, we present a design principle for broadband achromatic and polarization-insensitive metalenses using two sets of anisotropic nanofins based on phase change material $\text{Ge}_2\text{Sb}_2\text{Se}_4\text{Te}_1$. By limiting the rotation angles of all nanofins to either 0 deg or 90 deg, the metalens with a suitable numerical aperture constructed by this fashion allows for achromatic and polarization-insensitive performance across the wavelength range of 4–5 μm , while maintaining high focusing efficiency and diffraction-limited performance. We also demonstrate the versatility of our approach by successfully implementing the generation of broadband achromatic and polarization-insensitive focusing optical vortex. This work represents a major advance in achromatic metalenses and may find more applications in compact and chip-scale devices.

Keywords: metasurfaces; broadband achromatic metalenses; polarization insensitivity; phase change materials of $\text{Ge}_2\text{Sb}_2\text{Se}_4\text{Te}_1$.

Received Mar. 31, 2023; revised manuscript received Jun. 23, 2023; accepted for publication Jul. 5, 2023; published online Jul. 22, 2023.

© The Authors. Published by SPIE and CLP under a Creative Commons Attribution 4.0 International License. Distribution or reproduction of this work in whole or in part requires full attribution of the original publication, including its DOI.

[DOI: [10.1117/1.APN.2.5.056002](https://doi.org/10.1117/1.APN.2.5.056002)]

1 Introduction

Conventional refractive optical components, allowing precise control of the optical wavefront by relying on gradual phase accumulations as light propagates through bulky media, are generally bulky, costly, and time-consuming to manufacture with high precision, which significantly hinders their application, especially in miniaturized and highly integrated devices. In recent years, metasurfaces, consisting of subwavelength-spaced phase shifters at an interface, have emerged as a flexible platform for

shaping the wavefront by tailoring the phase, amplitude, and polarization at will, enabling the realization of various ultracompact optical components, ranging from lenses,^{1–6} holograms,^{7–10} and carpet cloaks^{11,12} to beam deflectors.^{13–15} Among these devices, metalenses, metasurfaces encoded with hyperbolic phase profiles, have attracted intense attention due to their great potential for future efficient portable or wearable optical devices with small footprints and light weights. However, current metalenses are mostly imparted with large chromatic aberration, mainly due to the resonant phase dispersion of constituent elements as well as distinct phase accumulations as light propagates in free space with different wavelengths, resulting in produced images that are blurred or fringed with color around the

*Address all correspondence to Junwei Xu, xujunwei001@zua.edu.cn; Zhi-Yuan Li, phzyli@scut.edu.cn

edges of objects. Hence, achromatic metalenses that compensate for chromatic aberrations within a wavelength range of interest are especially desirable.

To address this challenge, assorted approaches have been proposed and demonstrated. One is the confocal achromatic scheme for several discrete wavelengths, which is realized by compensating the propagation phase dispersion. For example, in 2015, Aieta et al. demonstrated a multiwavelength chromatic-free metalens by utilizing multiple coupled resonances to tailor phase profiles at several discrete frequencies.¹⁶ In 2016, Lin et al. demonstrated the feasibility of multiwavelength achromatic metalenses by capitalizing on developments in interleaved phased array antenna technology and gradient metasurfaces.¹⁷ However, the schemes did not achieve truly continuous broadband achromatic performance, and the achromatic bandwidth is hardly expanded due to the limited design freedom. In order to realize truly continuous broadband achromatic focusing, creative design principles need to be developed. In 2017, via dispersion engineering of dielectric phase shifters, Khorasaninejad et al. experimentally reported an achromatic metalens operating over a continuous bandwidth (60 nm) in the visible range.¹⁸ Arbabi et al. experimentally demonstrated zero-dispersion achromatic metalenses with a 140 nm bandwidth by simultaneously controlling the “effective refractive index” (phase profiles) and “chromatic dispersion” (wavelength derivative of phase profiles) of the meta-atoms.¹⁹ Unfortunately, the unfavorable achromatic bandwidths severely hinder their further potential applications. New substantial progress has been made in continuous broadband achromatic metasurface by Wang et al.²⁰ In contrast with the abrupt phase compensations caused by optical resonances, they implemented the achromatic metalenses in the wavelength range from 1200 to 1680 nm via the integrated resonance method (IRM), i.e., by elaborately designing the arrangement, shapes, and rotation angles of the resonators simultaneously to satisfy the phase and phase dispersion requirements. Due to the advantages of low cross talk, high efficiency, large numerical aperture (NA), and wide-spectrum achromatic focusing, the IRM has become mainstream for implementing achromatic metalenses.^{21–23} However, achromatic metalenses constructed by this designed method usually suffer from large polarization sensitivity.

Recent advances suggest such a challenge can be addressed by adopting symmetric nanostructures or their inverse nanostructures to constitute a metasurface,^{24–29} which, however, usually comes with the price of a vast of optimization effort and time consumption, and losing a degree of freedom in the design space due to the symmetry of these constituent elements. Most recently, Capasso’s group counterintuitively opened up an unprecedented solution to realize an achromatic metalens capable of focusing any incident polarization in the visible range by limiting the rotation angle of each anisotropic element to either 0 deg or 90 deg, which, however, still involves multitudinous optimization efforts.³ Ni’s group presented an inverse design approach that efficiently produces meta-atoms with unintuitive geometries required for broadband achromatic polarization-insensitive metalenses, but it still does not get rid of the constraints in terms of the constituent elements with high symmetry.³⁰

In this work, inspired by the Rayleigh criterion for spot resolution, we present a novel and generic design principle for broadband achromatic and polarization-insensitive metalenses (BAPIML) using two otherwise anisotropic nanofins (NFs)

based on phase-change materials of $\text{Ge}_2\text{Sb}_2\text{Se}_4\text{Te}_1$ (GSST). By limiting the rotation angles of the two sets of nanofins to either 0 deg or 90 deg, i.e., the two sets of anisotropic nanofins arranged orthogonally or parallel to each other, the metalens with a fine NA constructed in this fashion is endowed with achromatic and polarization-insensitive performance across the mid-wavelength infrared regime (MWIR) from the wavelength $\lambda = 4$ to $5 \mu\text{m}$, while maintaining high focusing efficiency (the highest efficiency is up to 43% and the averaged focusing efficiency is 34.9%) and diffraction-limited focusing performance. The generated spots within the operating wavelength range are focused at almost the same points with a slight variation (from 1.62% to 6.13% deviation relative to the pre-designed focal length), matching well with the theoretical values. In addition, we also demonstrate the versatility of our design approach by successfully implementing the generation of the broadband achromatic and polarization-insensitive focusing optical vortex (BAPIFOV) (with constant topological charge $l = 2$). This work represents an easy, feasible, and versatile route in designing broadband achromatic and polarization-insensitive metadevices and may find more applications in compact and chip-scale MWIR devices, such as molecular sensing or bioimaging, detectors, and holographic displays.

2 Principle and Methods

Figure 1(a) shows the schematic illustration of the BAPIML that enables a broadband incident beam with any polarization to be achromatically converged into a diffraction-limited spot. To implement such a BAPIML, several factors have to be considered. First, since any input polarization can be decomposed into a superposition of left-handed circularly polarized (LCP) and right-handed circularly polarized (RCP) lights, the metalens can be treated with the capacity of focusing any incident polarization, i.e., polarization insensitivity, as long as it simultaneously focuses the LCP and RCP incident beams into the same spot. To focus the LCP incidence into a converged spot at (x_L, y_L, f_L) , each meta-atom of metadevices should be encoded with a phase profile φ_{LCP} governed by

$$\varphi_{\text{LCP}} = \frac{2\pi}{\lambda} \left[f_L - \sqrt{(x - x_L)^2 + (y - y_L)^2 + f_L^2} \right] + l_L \cdot \arctan\left(\frac{y}{x}\right). \quad (1)$$

Accordingly, the phase profile φ_{RCP} for the metadevices that can converge the RCP incidence into a diffraction-limited spot at (x_R, y_R, f_R) needs to follow^{31–33}

$$\varphi_{\text{RCP}} = -\frac{2\pi}{\lambda} \left[f_R - \sqrt{(x - x_R)^2 + (y - y_R)^2 + f_R^2} \right] + l_R \cdot \arctan\left(\frac{y}{x}\right), \quad (2)$$

where f_L/f_R represents the focal length, l_L/l_R denotes the topological charge of the converged beams, and λ is the operating wavelength. Therefore, the total phase distributions for a spin-decoupled metadvice that can simultaneously focus the LCP and RCP components into a diffraction-limited spot can be expressed as^{31–33}

$$\varphi_{\text{total}} = \arg [\exp(i * \varphi_{\text{LCP}}) + \exp(i * \varphi_{\text{RCP}})]. \quad (3)$$

It should be noted that the rotation angle of each element is restricted to either 0 deg or 90 deg when the phase spectra for LCP and RCP incidences are imposed with the same focal length ($f_L = f_R$), zero topological charge ($l_L = l_R = 0$), and the reference positions right at the origin ($x_L = x_R = 0$, $y_L = y_R = 0$), which is exactly the underlying origin of polarization insensitivity for metalenses. It can be understood from the Pancharatnam–Berry (PB) phase.^{34,35} When a circularly polarized (CP) beam $\left(\begin{bmatrix} 1 \\ \pm i \end{bmatrix}\right)$ passes through a nanofin, the transmitted electric field $\left(\begin{bmatrix} E_x \\ E_y \end{bmatrix}\right)$ can be written by Jones vector,

$$\begin{bmatrix} E_x \\ E_y \end{bmatrix} = \frac{t_l + t_s}{2} \begin{bmatrix} 1 \\ \pm i \end{bmatrix} + \frac{t_l - t_s}{2} \exp(\pm i2\alpha) \begin{bmatrix} 1 \\ \mp i \end{bmatrix}, \quad (4)$$

where t_l and t_s denote complex transmission coefficients upon the normalized incidence polarizing along the long and short axes of the nanofins, respectively. The α is the rotation angle of nanofins with respect to the x axis. When $t_l = -t_s = 1$, the undesirable scatterings caused by the first term of Eq. (4) can be eliminated, and the polarization conversion efficiency (PCE) stemming from the second term of Eq. (4) can be maximized, thus ensuring the nanofins behave as a perfect half-wave plate. The $\exp(\pm i2\alpha)$ in the second term elucidates the origin of PB phase (φ^{PB}). Considering $\varphi_{\text{LCP}}^{\text{PB}} = \varphi_{\text{RCP}}^{\text{PB}} = 2\alpha$, the values of $\exp(i2\alpha)$ and $\exp(-i2\alpha)$ will be identical if the nanofins are arranged with $\alpha = 0$ deg or $\alpha = 90$ deg, resulting in the same phase profile yielded by both RCP and LCP incidence interacting with a metalens composed of nanofins arranged parallel or perpendicular to each other, which allows for the metalens capable of focusing any incident polarization.

In general, due to the variation in the effective refractive index of the material, refractive lenses will deflect the incidence with longer wavelengths at a smaller angle and thus perform smaller focal lengths, or vice versa, which results in large chromatic aberration when a refractive lens interacts with the incidence across a broadband wavelength range. Conventional metalenses also suffer from the same puzzle, pronouncedly degrading their focusing and imaging performance, which is another issue that has to be addressed. Previous achromatic metadevices mostly utilized the IRM to fulfill the required phase and its dispersion (group delay and group delay dispersion). However, this approach is usually at the expense of countless design/optimization effort and time consumption. Here, inspired by the Rayleigh criterion for spot resolution, we proposed an unprecedented solution toward achromatic metadevices. Two sets of half-plate-behavior anisotropic nanofins (NF1 and NF2) are selected as constitutive elements for the designed metadevice, in which NF1 works well for $\lambda_1 = 4 \mu\text{m}$ and NF2 for $\lambda_2 = 5 \mu\text{m}$. By eliminating the focus offset to zero ($x_L = x_R = 0$ and $y_L = y_R = 0$) and setting the same focal length to $f_L = f_R = f_0$, the rotation angle of each element (NF1 and NF2) is restricted to either 0 deg or 90 deg, which results in NF1 to be perpendicular or parallel to NF2, and thus forming the “cross” (orthogonal mode) or “straight” (parallel mode) superunit nanostructure (NF1&NF2) in our design. Therefore, the designed BAPIML can be viewed as a hybridization of the NF1-based metalens (ML1) and the NF2-based

metalens (ML2), where ML1 shares the same focal length ($f_L = f_R = f_0$) with ML2. Both ML1 and ML2 are PB phase-assisted metalenses, manifesting broadband but diffractive focusing features.

Benefiting from the reality of “The longer the wavelength, the shorter the focal length” for diffractive metalenses, we counterintuitively designed a hybridized metalens composed of ML1 and ML2, in which the focusing behavior of ML1 can fully compensate for the dispersion caused by ML2 over the entire interested wavelength range (from λ_1 to λ_2), or vice versa, through fine design of their NAs (corresponding to the radius and focal length of metalenses). Consequently, our metalens design enables broadband achromatic focusing performance. This can be vividly interpreted by the idea of the Rayleigh criterion for spot resolution. For a specific wavelength of λ_i ($\lambda_1 < \lambda_i < \lambda_2$) and the preset focal length of f_0 , the bright spots generated by ML1 and ML2 are, respectively, focused at two separated positions along the z axis, in which one is larger than f_0 , while the other is smaller than f_0 . When the distance between the centers of the two foci is large enough, the two bright spots can be clearly distinguished [Fig. 1(b)]. As the distance between their centers gradually decreases, the two bright spots move toward each other until they can be just distinguished [Fig. 1(c)]. By further decreasing the distance between their centers, two bright spots are fully merged into one single spot that cannot be unrecognizable and indistinguishable to the naked eye [Fig. 1(d)], which is exactly the achromatic strategy we adopted: by ingeniously designing parameters (the radius and focal length of metalenses), the two bright spots facing all interested wavelengths are fully merged into one single focusing spot, resulting in the focal lengths of the metalens design under the incidence, with all the interested wavelengths basically unchanged (f_0).

The building blocks of metalenses are composed of two sets of GSST-based nanofins, NF1 and NF2, setting on a CaF_2 substrate, as illustrated in the inset of Fig. 1(a). For the optimization of the meta-atoms, we perform full-wave finite-element simulations at working wavelengths of 4 and 5 μm , respectively. Periodic boundary conditions were implemented at both x and y directions and two periodic ports were set along the z axis. The circularly polarized incident light is illuminated on the meta-atom from the substrate side (the lower port), and the amplitude is probed for the transmitted light with the opposite helicity (T_{cross}). GSST was selected as a nanostructure material mainly due to its large index contrast with respect to the CaF_2 substrate as well as excellent transmittance and low loss characteristics in the mid-wavelength infrared range. The wavelength-dependent optical constants of GSST can be seen in the experimental data in Refs. 36–38, while the refractive index of CaF_2 was taken as 1.47 at the operating wavelength range. Unless otherwise specified, GSST remains its amorphous state (aGSST) in simulations by default. To perform broadband achromatic focusing merit, NF1 and NF2 are arranged parallel or perpendicular to each other. NF1 with length L_1 and width W_1 share the same height of $h = 4.2 \mu\text{m}$ with NF2 that is equipped with length L_2 and width W_2 . Through sweeping the parameters of NF1 for $\lambda_1 = 4 \mu\text{m}$ and NF2 for $\lambda_2 = 5 \mu\text{m}$, $L_1 = 0.95 \mu\text{m}$, $W_1 = 0.6 \mu\text{m}$, $L_2 = 0.45 \mu\text{m}$, and $W_2 = 1.65 \mu\text{m}$ were selected and the optimal meta-atoms with the “cross” (orthogonal mode) or “straight” (parallel mode) superunit nanostructure are arranged into a square with a periodicity $p = 3 \mu\text{m}$. To better cater to the function of a cylindrical lens, the arrangement of

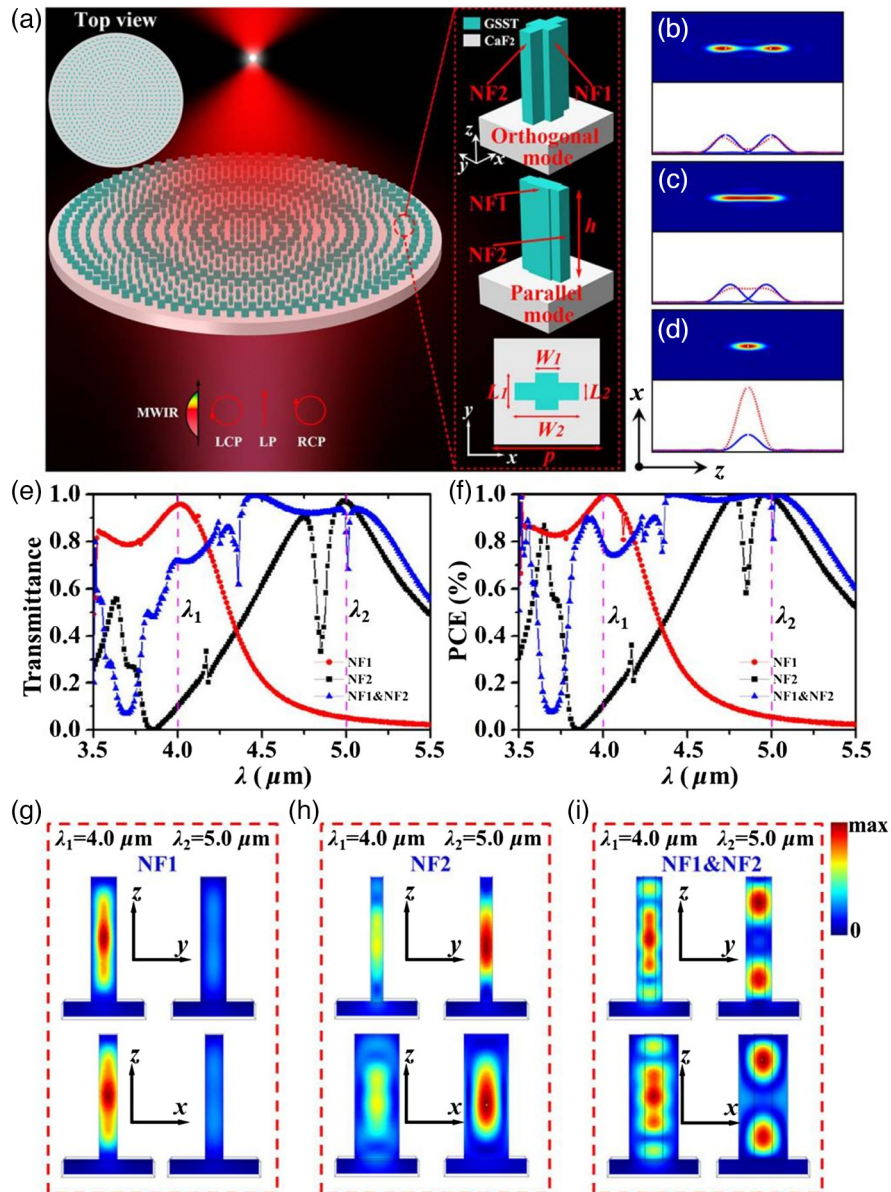


Fig. 1 Artistic rendering and design principles of the proposed BAPIML. (a) Schematic illustration of the BAPIML with broadband achromatic and polarization-insensitive functions. The MWIR beams with arbitrary polarizations are normally illuminated on the metasurface from the substrate side and the transmitted light with opposite helicity is achromatically converged at the same spot. The insets exhibit the top view of circular configuration of the BAPIML (left side) and the schematic diagram of the constituent elements of the BAPIML (right side). The meta-atom consists of two anisotropic GSST-based nanofins (NF1 and NF2) arranged orthogonally (orthogonal mode) or in parallel (parallel mode) to each other standing on the CaF₂ substrate. The optimal structural parameters are $p = 3 \mu\text{m}$, $h = 4.2 \mu\text{m}$, $L_1 = 0.95 \mu\text{m}$, $W_1 = 0.6 \mu\text{m}$, $L_2 = 0.45 \mu\text{m}$, and $W_2 = 1.65 \mu\text{m}$, respectively. (b)–(d) Design principles of the proposed BAPIML: the diagram of overlapping process of two bright spots along the z axis. The cross-polarization transmittance (T_{cross}) in (e) and the corresponding PCE with respect to the wavelength in (f) for the selected nanofins of NF1 (black lines), NF2 (red lines), and their composite body NF1 and NF2 (blue lines). (g)–(i) Normalized magnetic intensity profiles for the selected nanofins of NF1, NF2, and their composite body NF1&NF2 along the x -cut (top panel) and y -cut (bottom panel) both at $\lambda_1 = 4 \mu\text{m}$ and $\lambda_2 = 5 \mu\text{m}$, respectively.

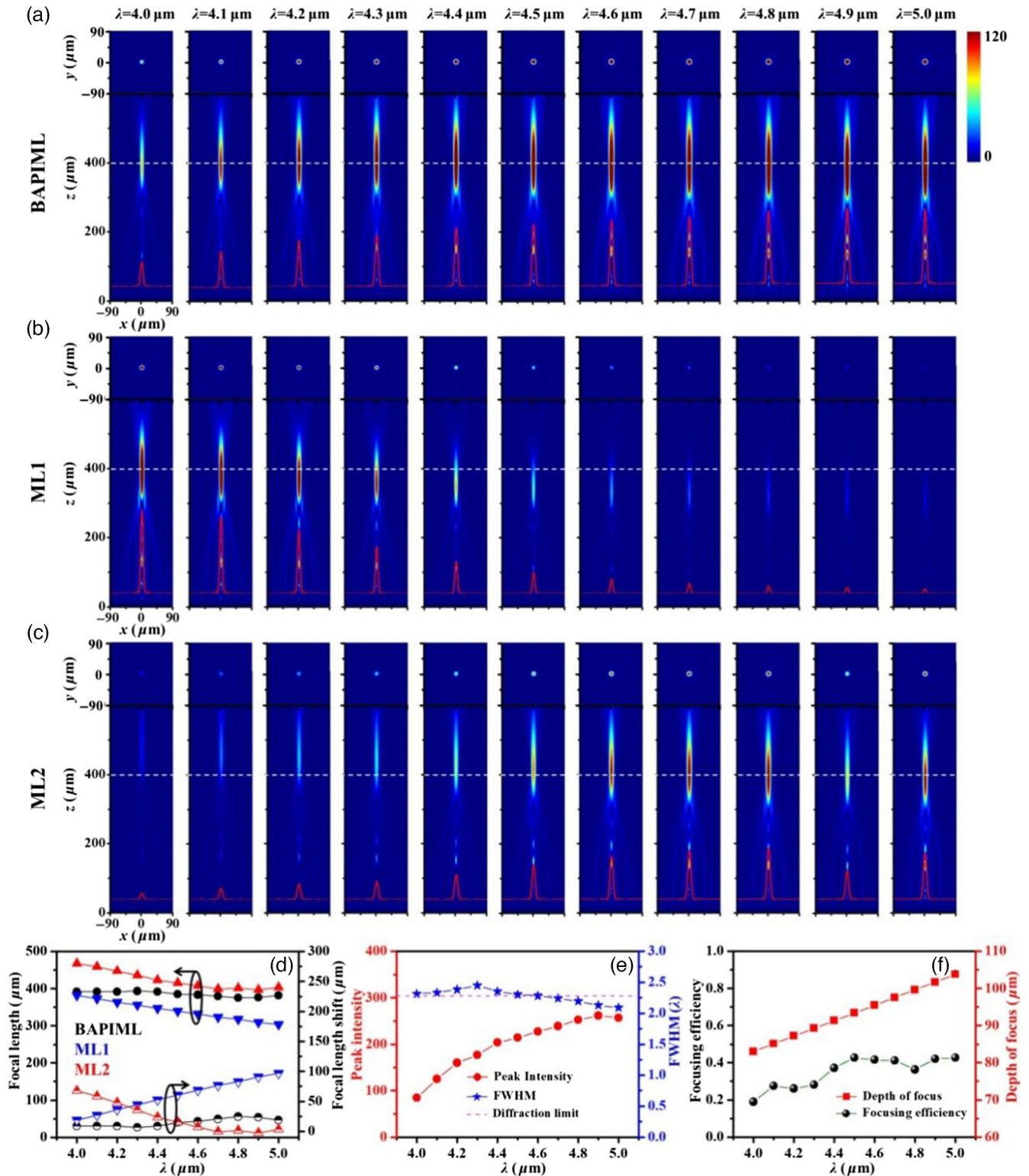


Fig. 2 Broadband achromatic focusing characterization of the BAPIML. The BAPIML was constructed with an $\text{NA} = 0.22$ and a focal length of 400 μm . As control samples, the chromatic metalenses of ML1 and ML2 with the same NA and focal length were also designed. (a)–(c) Simulated intensity distributions in the $x - z$ planes (bottom panels) and z -cut field profiles at focal planes (top panels) for the designed BAPIML, ML1 and ML2 under LCP incidence across the MWIR of 4 to 5 μm with a step of 0.1 μm , respectively. The insets (red solid lines) represent normalized intensity profiles along the white dashed lines of (a)–(c) for the three metalenses. The position of the dashed lines corresponds to the predefined focal length of 400 μm . (d) Simulated focal lengths

Fig. 2 (Continued) and focal length shifts functioning versus wavelength for the designed BAPIML. The cases for the ML1 and ML2 are also given as comparisons. (e) The simulated peak intensities and FWHMs of focal spots as a function of the sampled wavelengths for the designed BAPIML. The pink dashed line denotes the corresponding theoretical diffraction limits. (f) The simulated focusing efficiencies and depth of focus of focal spots versus the sampled wavelengths for the designed BAPIML.

the proposed metalenses was optimized into a circular configuration [see Fig. 1(a)], in which the interval of nanostructures within the circle was $3 \mu\text{m}$ (period of meta-atoms). Numerical simulations of the metalenses were carried out by the commercial software Lumerical Solutions. In the simulation, perfectly matched layers are set around the model, and the plane wave excitations with specific polarization along the z axis acts as the excitation source and the output electric field with opposite helicity are probed by the monitors set on the metasurface. According to the reported work,³⁶ a prototype of the proposed metalens can be realized by patterning the thermally evaporated GSST films on a CaF_2 substrate using electron beam lithography followed by standard plasma etching.

Figure 1(e) shows the numerically calculated transmittance (T_{cross}) across the wavelength range from 3.5 to $5.5 \mu\text{m}$ for three associated meta-atoms, respectively, based on NF1, NF2, and NF1&NF2 (combinations of NF1 and NF2). The normalized transmittance spectra reveal that the NF1-based meta-atom is resonant around $\lambda_1 = 4 \mu\text{m}$ accompanied by a peak value above 0.95 , whereas the NF2-based meta-atom has tiny transmittance (<0.1) at this spectral position. The opposite phenomenon happens at $\lambda_2 = 5 \mu\text{m}$, i.e., the NF2-based meta-atom appears resonant at $\lambda_2 = 5 \mu\text{m}$ with the peak value up to 0.97 , while the NF1-based meta-atom's transmittance decreases to be <0.05 at this site. More critically, the transmittance yielded by NF1&NF2-based meta-atom remains at fairly high levels, despite some negligible dip, and the average transmittance reaches up to 0.88 within the entire interested wavelength range from 4 to $5 \mu\text{m}$, which is the key to realizing broadband and efficient achromatic focusing. By checking the normalized magnetic field distributions along the x -cut (top panel) and y -cut (bottom panel) planes, as shown in Figs. 1(g)–1(i), the high transmittance obtained by NF1-based meta-atom at $\lambda_1 = 4 \mu\text{m}$, NF2-based meta-atom at $\lambda_2 = 5 \mu\text{m}$, and NF1&NF2-based meta-atom both at $\lambda_1 = 4 \mu\text{m}$ and $\lambda_2 = 5 \mu\text{m}$ can be attributed to the excitation of multi-resonances inside the NFs at the corresponding wavelengths. In addition, we also calculated the PCE, defined as $\text{PCE} = T_{\text{cross}} / (T_{\text{cross}} + T_{\text{co}})$ ($T_{\text{cross}}/T_{\text{co}}$ is the cross/co-polarized transmitted component), shown in Fig. 1(f), which exhibits excellent agreement with the corresponding transmittance, further confirming the feasibility of the unit structure design.

3 Results and Discussion

As a proof-of-concept demonstration, we designed an NF1&NF2-based BAPIML, and two other metalenses are also constructed with NF1 (labeled by ML1) and NF2 (labeled by ML2), respectively, for comparison. All three metalenses possess the same radius (R) of $90 \mu\text{m}$ (circular footprint of $\pi \times 90 \mu\text{m} \times 90 \mu\text{m}$) and an identical focal length of $f_L = f_R = 400 \mu\text{m}$, yielding the $\text{NA} = 0.22$. Figure 2(a) shows the simulated cross-sectional intensity profiles for the designed BAPIML upon LCP illumination within the wavelength range

from 4 to $5 \mu\text{m}$, in which the top panel shows the z -cuts intensity profiles at focal planes and the bottom panel plots the intensity profiles at the $x - z$ planes, respectively. One can witness that the centers of bright spots hatched by the BAPIML design are all close to the predefined position (labeled by a white dashed line). Comparisons of the focal spots in terms of cross-sectional intensity profiles are also plotted in Fig. 2(b) (ML1) and Fig. 2(c) (ML2), revealing that the ML1 and ML2 can also converge the incident beams within 4 to $5 \mu\text{m}$ waveband into bright spots. However, these focal spots exhibit wavelength-dependent focal length and intensity caused by the dispersion nature inherited from ML1 and ML2.

To quantitatively characterize the focusing performance, Fig. 2(d) shows the focal lengths and focal length shifts as a function of incident wavelengths for three metalenses. The focal length shift is defined as the deviation of the actual focal length from the preset focal length. Clearly, for the BAPIML across the entire wavelength range from 4 to $5 \mu\text{m}$, all focal lengths remained almost unchanged around the predetermined focal length, resulting in the negligible focal length shifts ($<6.13\%$ variation) compared with the corresponding depth of focus [λ/NA^2 , as shown in Fig. 2(f)]. However, these situations are not so positive for both ML1 and ML2. Due to the inherent dispersion, both ML1 and ML2 exhibit monotonically decreasing focal lengths accompanied by respective maximum focal length shifts up to 96 and $68 \mu\text{m}$ as the incidence redshifts from 4 to $5 \mu\text{m}$, fitting well to those of the diffractive lens, of which the focal length $f(\lambda)$ is basically governed by $f(\lambda) = f(\lambda_i)(\lambda_i)/\lambda$.³⁹ $f(\lambda_i)$ denotes the focal length when the incident light with preset target wavelength λ_i interacts with the metalenses. It should be noted that ML1 works well at $\lambda_1 = 4 \mu\text{m}$, while ML2 plays a strong role at $\lambda_2 = 5 \mu\text{m}$.

In addition, we also evaluate the quality of the focal spots for the BAPIML by extracting the peak intensity and full width at half-maximums (FWHMs) across all the sampled wavelengths, as shown in Fig. 2(e). The peak intensity presents an upward trend by increasing the incident wavelength, which may be attributed to the transition from higher-order (low-energy) to lower-order (high-energy) resonance modes for the superunit nanostructure (NF1&NF2) [shown in Fig. 1(g)]. The FWHMs that are extracted from the x -cuts intensity profiles across the focal spots in the insets of Fig. 2(a) show the focal spots are nearly diffraction-limited for the BAPIML for all the sampled wavelengths. Figure 2(f) also shows the calculated focusing efficiency for the BAPIML, which is defined as the ratio of the optical power enclosed in a $3 \times \text{FWHM}$ area of the focal spot to the optical power of the incident beam. The focusing efficiency basically presents a monotonically increasing trend, despite some perturbations as the incident wavelength increases. The highest efficiency reaches up to 43% , and the averaged efficiency is about 34.9% over the entire operating bandwidth. The variation of the focusing efficiency can probably stem from the transmission amplitude change and the nearest-neighbor

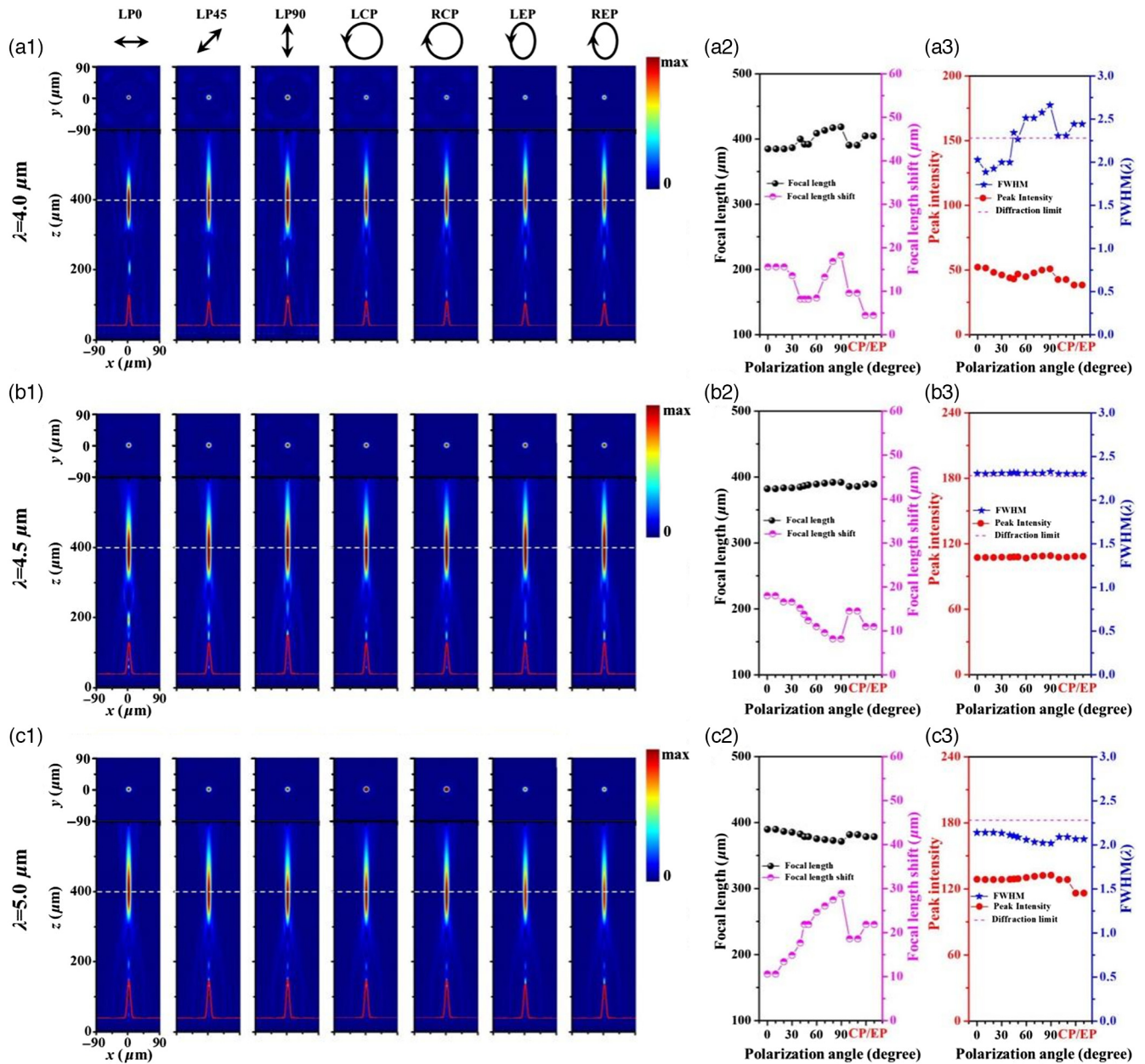


Fig. 3 Polarization-insensitive focusing performance of the BAPIML. Simulated intensity profiles in the $x - z$ planes (bottom panels) and z -cut field profiles at the focal planes (top panels) for the designed BAPIML under linearly, circularly, and elliptically polarized lights at (a1) $\lambda_1 = 4 \mu\text{m}$, (b1) $\lambda_{\text{mid}} = 4.5 \mu\text{m}$, and (c1) $\lambda_2 = 5 \mu\text{m}$, respectively. Herein LP0, LP45, and LP90 represent linearly polarized incident lights with electric vectors polarized in 0 deg, 45 deg, and 90 deg relative to the $+x$ axis, and LEP and REP denote left-handed and right-handed elliptically polarized light with ellipticity of ± 0.5 , respectively. Simulated focal length and focal length shifts functioning versus the incident polarization states for the BAPIML at (a2) $\lambda_1 = 4 \mu\text{m}$, (b2) $\lambda_{\text{mid}} = 4.5 \mu\text{m}$, and (c2) $\lambda_2 = 5 \mu\text{m}$, respectively. Simulated peak intensities and FWHMs of focal spots as a function of the incident polarization states for the designed BAPIML at (a3) $\lambda_1 = 4 \mu\text{m}$, (b3) $\lambda_{\text{mid}} = 4.5 \mu\text{m}$, and (c3) $\lambda_2 = 5 \mu\text{m}$, respectively. The pink dashed lines denote the corresponding theoretical diffraction limits. The number on the abscissa represents the polarization angles of linearly polarized incident light and CP/EP represents circularly/elliptically polarized incident light.

effects.²⁹ We note that the focusing efficiencies of the BAPIML are not fully on par with monochromatic designs,^{4,40,41} however, they are comparable and even outperform other recent dielectric achromatic metalens demonstrations.^{1,20,30,42}

Conferring broadband achromatic metalens with polarization-insensitive focusing characteristics is highly desirable for many applications, especially in imaging fields. However, current solutions appear to limit the choice of their constituent

elements to isotropic nanostructures, consequently losing a degree of freedom available in design parameters. Here, by limiting the rotation angles of the two sets of anisotropic nanofins either to 0 deg or 90 deg, we implement a broadband achromatic and polarization-insensitive metalens across the MWIR of $\lambda = 4$ to $5 \mu\text{m}$ by simulations. As a proof-of-concept demonstration, we show the simulated intensity profiles along axial plane for the designed BAPIML under 0-, 45-, 90-deg linearly polarized (LP0, LP45, and LP90) light, left-handed and right-handed elliptically polarized (LEP and REP) light with ellipticity of ± 0.5 ,

LCP and RCP light, respectively, upon three selected sampled wavelengths ($\lambda_1 = 4 \mu\text{m}$, $\lambda_{\text{mid}} = 4.5 \mu\text{m}$, and $\lambda_2 = 5 \mu\text{m}$) in Figs. 3(a1)–3(c1). It can be observed that bright spots with centers on almost the same focal lengths are generated by the BAPIML under different incident polarization states upon all the three selected sampled wavelengths. By quantitatively analyzing the focal lengths and the corresponding focal length shifts [as shown in Figs. 3(a2)–3(c2)], we find that the simulated focal lengths show a minor discrepancy (from 2.6% to 6.8% relative to the predefined focal length), robustly confirming

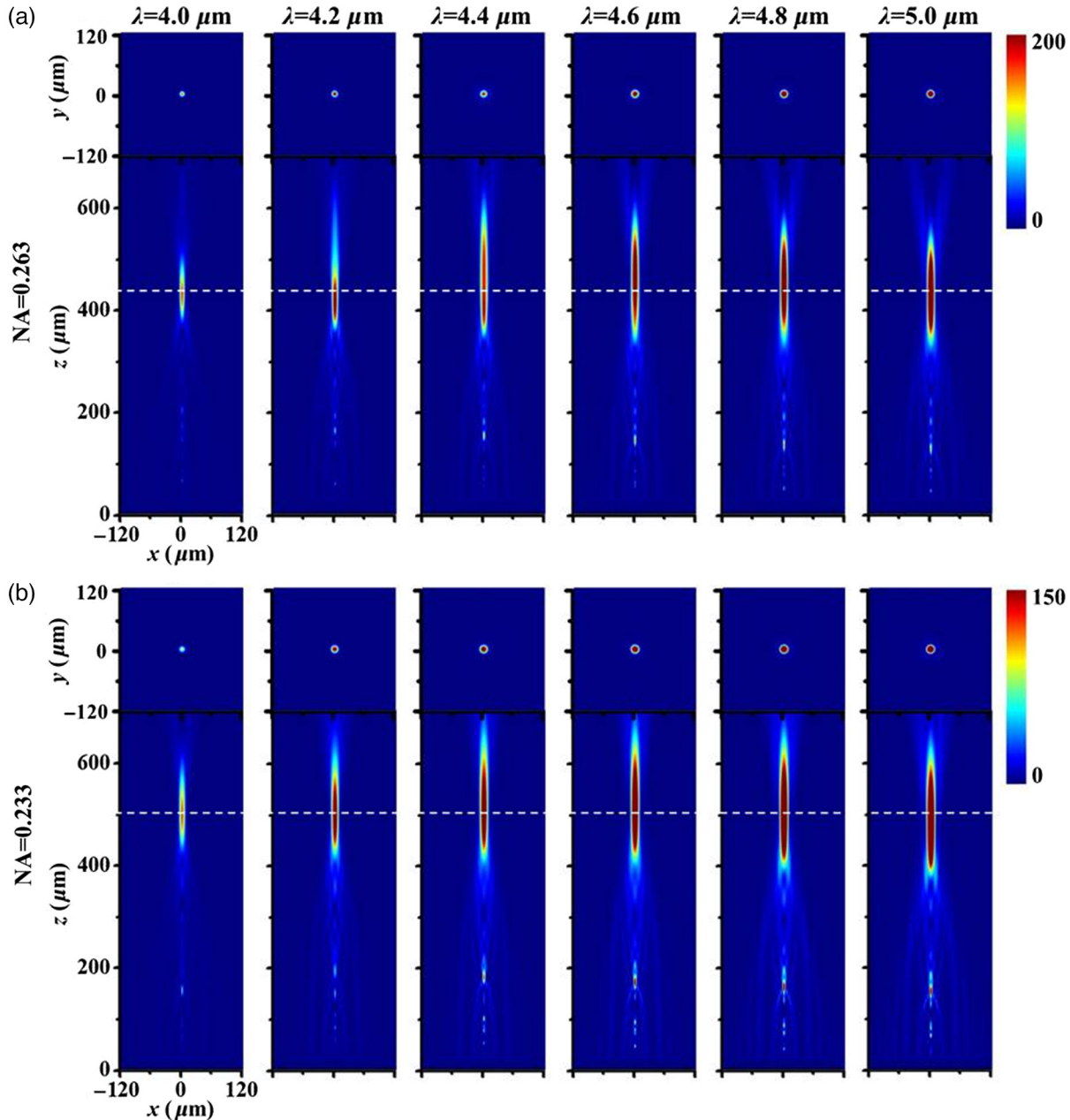


Fig. 4 Demonstration of the universality of our proposed design strategy. Simulated intensity profiles in the $x - z$ planes (bottom panels) and z -cut field profiles at the focal planes (top panels) for another two BAPIML designs with different NAs and focal lengths. (a) is for the BAPIML with $\text{NA} = 0.263$ and focal length is $440 \mu\text{m}$; (b) is for the other BAPIML with $\text{NA} = 0.233$ and focal length is $500 \mu\text{m}$. The white dashed lines indicate the positions of the preset focal lengths.

the broadband achromatic and polarization-insensitive focusing behavior of the BAPIML design. We also characterized the quality of the focal spots for the BAPIML under different incident polarization states upon each selected sampled wavelength, as shown in Figs. 3(a3)–3(c3). The results exhibit the almost-unchanged peak intensity and the nearly diffraction-limited focusing behaviors, further proving the BAPIML design indeed enables achromatic focusing under all the incident polarization states.

In addition, another two BAPIML designs with different NAs ($R = 120 \mu\text{m}$, $f_L = f_R = 440 \mu\text{m}$ for $\text{NA} = 0.263$, and

$R = 120 \mu\text{m}$, $f_L = f_R = 500 \mu\text{m}$ for $\text{NA} = 0.233$) based on the proposed method are presented; their focusing performance is shown in Fig. 4. From the simulated cross-sectional intensity profiles shown in the bottom panel of Figs. 4(a) and 4(b), one can observe that the centers of bright spots generated by the two BAPIMLs keep almost unchanged around the predefined focal length across the wavelength range from 4 to 5 μm . Together with the corresponding z -cuts field profiles of the bright spots shown in top panel of Figs. 4(a) and 4(b), we can infer that both the two BAPIMLs can also realize broadband achromatic and the nearly diffraction-limited focusing merits, as well as

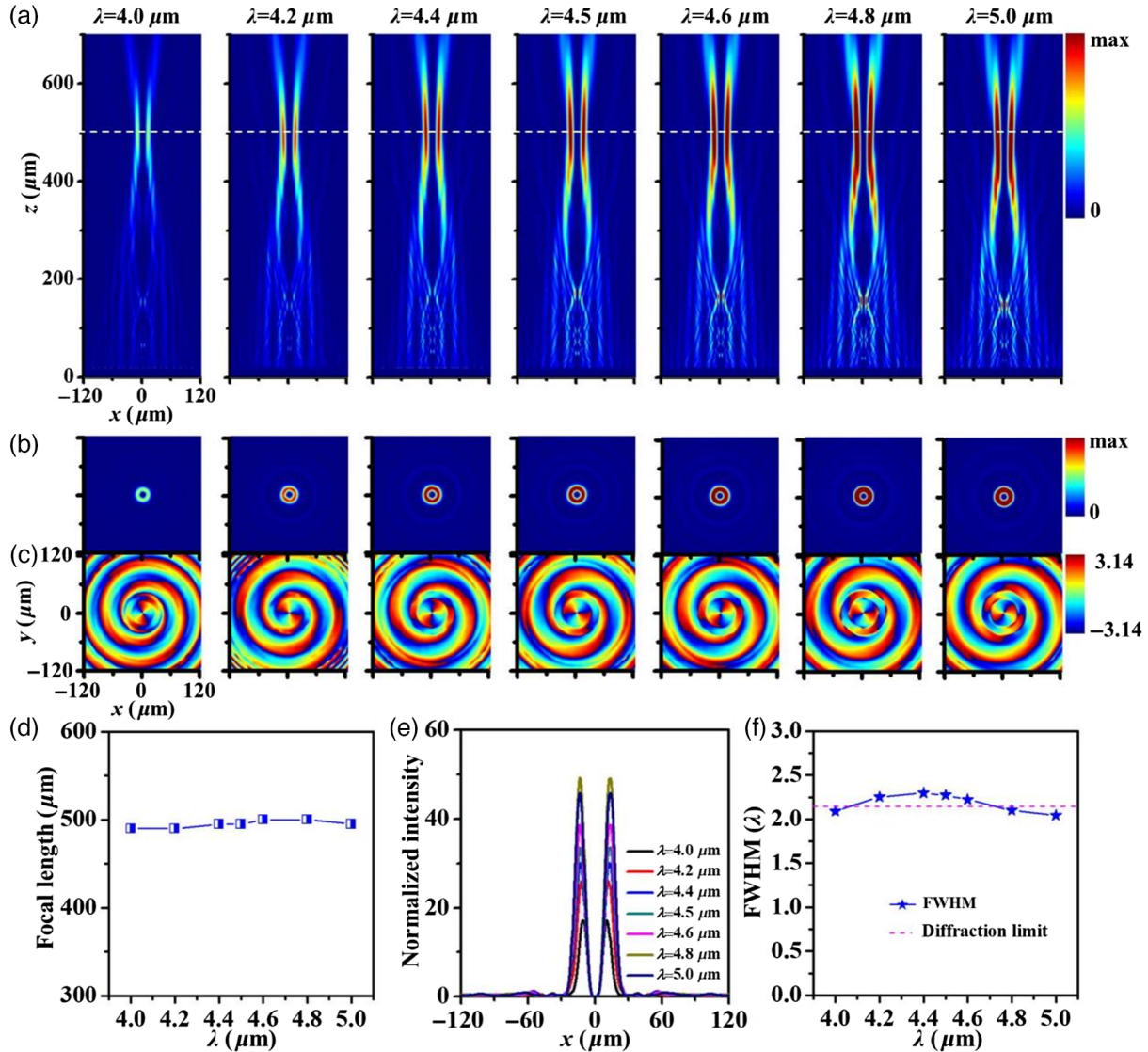


Fig. 5 Broadband achromatic focusing characterizations of the BAPIFOV. (a) Simulated intensity profiles along the axial plane within the overall designed waveband from 4 to 5 μm for the BAPIFOV under LCP incident light. (b) Simulated transverse intensity distributions and (c) phase profiles along the white dashed lines plotted in (a) for each sampled wavelength. (d) Simulated focal length versus the sampled wavelengths for the designed BAPIFOV. (e) Simulated horizontal cuts intensity profiles of the focal spots at the focal planes across the entire designed waveband from 4 to 5 μm for the BAPIFOV under LCP incident light. The hump-like field distributions along with intensity singularity (zero intensity) right in the center prove the focusing behavior of the vortex beam yield by the BAPIFOV meta-device. (f) Simulated FWHM spectra together with the theoretical diffraction limits versus the sampled wavelengths.

polarization-insensitive focusing performance (not shown here for simplicity), fully proving the universality of the design strategy despite some restrictions on NA in practical implementation.

To verify the versatility of our design strategy, a BAPIFOV generator is proposed and demonstrated by setting $f_L = f_R = 500 \mu\text{m}$, $x_L = x_R = 0$, $y_L = y_R = 0$, and $l_L = l_R = 2$ in

Eqs. (1) and (2). It should be noted that the rotation angle of each element (NF1 and NF2) is no longer limited to either 0 deg or 90 deg due to the existence of azimuth coordinates $[l_{L/R} \times \arctan(y/x)]$. However, NF1 always remains perpendicular or parallel to NF2, which ensures the polarization-insensitive performance of our metadvice. The BAPIFOV metadvice has a radius of $120 \mu\text{m}$ and an NA value of

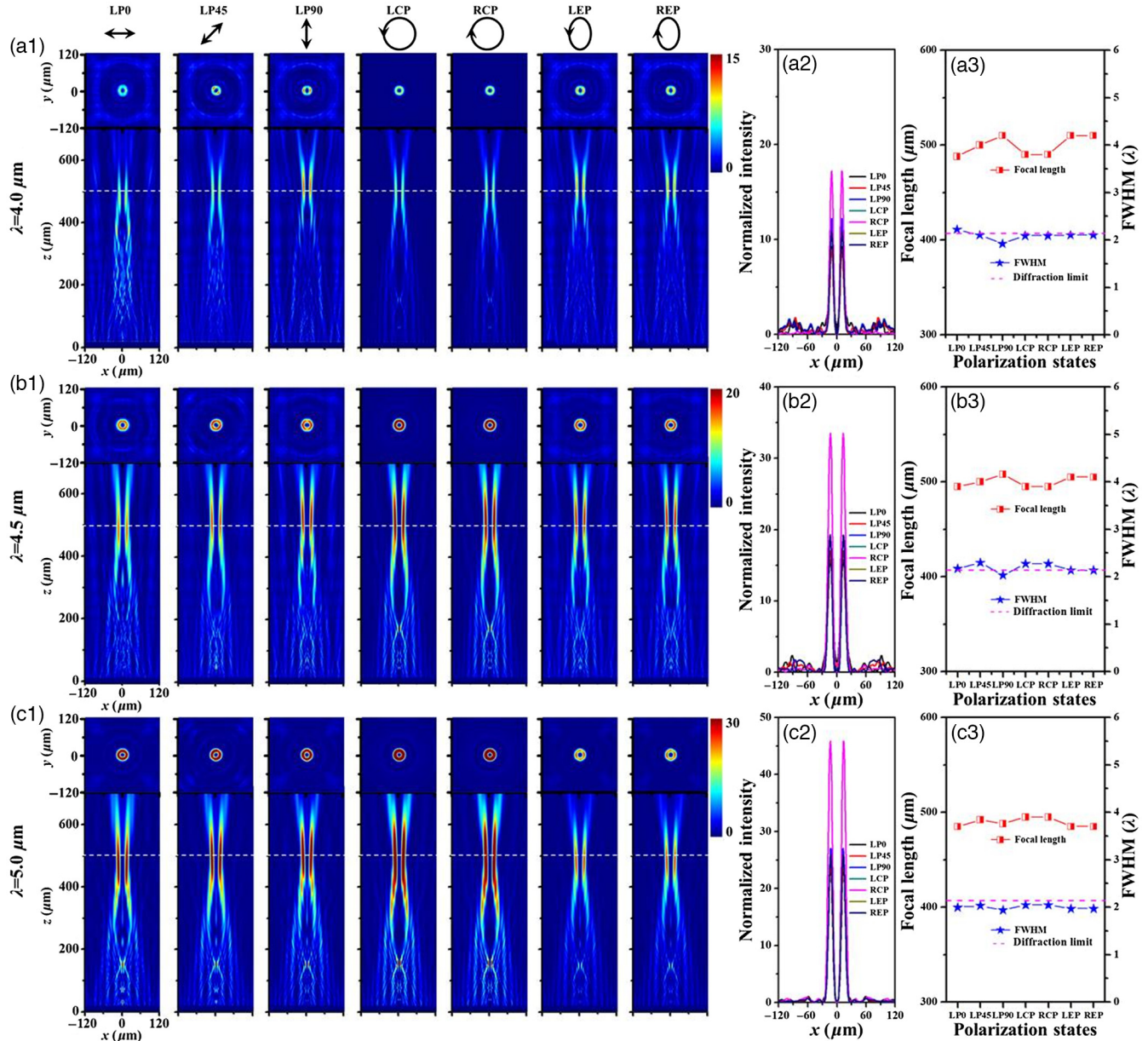


Fig. 6 Polarization-insensitive characterization of the BAPIFOV. Simulated intensity profiles along the axial plane (bottom panel) and z-cut field profiles at the focal planes (top panels) for the BAPIFOV under linearly, circularly, and elliptically polarized incident lights at (a1) $\lambda_1 = 4 \mu\text{m}$, (b1) $\lambda_{\text{mid}} = 4.5 \mu\text{m}$, and (c1) $\lambda_2 = 5 \mu\text{m}$, respectively. The white dashed lines indicate the positions of the preset focal lengths ($500 \mu\text{m}$). Simulated horizontal cuts intensity profiles of the focal spots at the focal planes for the BAPIFOV under all the sampled incident polarizations at (a2) $\lambda_1 = 4 \mu\text{m}$, (b2) $\lambda_{\text{mid}} = 4.5 \mu\text{m}$, and (c2) $\lambda_2 = 5 \mu\text{m}$, respectively. Simulated focal lengths (red lines) and FWHMs (blue lines) of focal spots versus the incident polarizations for the designed BAPIFOV at (a3) $\lambda_1 = 4 \mu\text{m}$, (b3) $\lambda_{\text{mid}} = 4.5 \mu\text{m}$, and (c3) $\lambda_2 = 5 \mu\text{m}$, respectively. The pink dashed line denotes the corresponding theoretical diffraction limits.

0.233. Figure 5(a) shows the simulated electric intensity profiles in the $x - z$ plane for the BAPIFOV metadvice under the LCP illumination. It can be seen that two symmetrically distributed focal spots with centers on almost the same focal lengths are successfully hatched by the BAPIFOV metadvice across the entire interested wavelength range of 4–5 μm . Accompanied by the corresponding z -cuts doughnut-shaped electric field distributions at the focal planes shown in Fig. 5(b), we can deduce that the BAPIFOV metadvice has the capacity of achromatically focusing the incident LCP light into a converged vortex beam across the wavelength range from $\lambda = 4$ to 5 μm . By analyzing the phase distributions at the focal planes shown in Fig. 5(c), we can identify the topological charge is 2, which is in good agreement with the theoretical design. To better illustrate the generated beams, the simulated focal lengths as a function of incident wavelength are plotted in Fig. 5(d), which shows that minor discrepancy (maximum 2.6% derivation relative to the predefined focal length) is produced by the BAPIFOV metadvice across all the sampled wavelengths. Figure 5(e) shows the horizontal (white dashed line) cuts intensity profiles across the focal spots for the BAPIFOV metadvice upon different incident wavelengths. The hump-like field distributions along with intensity singularity (zero intensity) right in the centers prove the focusing behavior of the vortex beam yielded by the BAPIFOV metadvice. Figure 5(f) summarizes the corresponding FWHM spectrum together with the theoretical diffraction limits for comparison. These results again confirm that the designed BAPIFOV metadvice allows for the implementation of broadband achromatic and nearly diffraction-limited focusing vortex beams.

We further study the focusing characteristics of the BAPIFOV metadvice under different polarized incidences for three selected sampled wavelengths ($\lambda_1 = 4 \mu\text{m}$, $\lambda_{\text{mid}} = 4.5 \mu\text{m}$, and $\lambda_2 = 5 \mu\text{m}$) shown in Figs. 6(a1)–6(c1), which reveal that the converged vortex beams with doughnut-shaped electric field profiles are successfully produced by the BAPIFOV metadvice under all concerned polarizations for the three selected sampled wavelengths. Figures 6(a2)–6(c2) illustrate the corresponding horizontal (white dashed line) cuts intensity profiles across the focal spots for BAPIFOV metadvice under all concerned polarizations for the three selected sampled wavelengths. The hump-like field distributions along with zero intensity singularity (zero intensity) right in the center further verify the BAPIFOV metadvice could work well upon all incident polarizations. Moreover, from Figs. 6(a3)–6(c3), we can observe there are almost no deviations (the maximum deviation is not more than 3%) in terms of actual focal length with respect to the predefined focal length and all the calculated FWHMs are very close to the diffraction limit for the BAPIFOV metadvice under all polarizations, definitely confirming the polarization-insensitive and nearly diffraction-limited focusing behavior of the BAPIFOV metadvice. The realization of broadband achromatic and polarization-insensitive focusing vortex beam generators may find many potential applications, such as biomedical nanochips, quantum key distribution in the MWIR, and other possible applications yet to be explored.

4 Conclusions

In fact, our design strategy inherently involves a trade-off between the operating bandwidth and the NA of metalenses, which limits the ability of metadvice to achieve wide achromatic

ranges and large NAs simultaneously. However, depending on specific application demands, we can sacrifice some degree of NA to obtain ultrabroadband achromatic metalenses or sacrifice a certain degree of achromatic range to obtain large-NA metalenses. It is worth noting that the designed metalens efficiency (43% and 34.9% are the highest and averaged efficiency, respectively) shown in Fig. 2(f) has not exhibited significant superiority compared to other dielectric achromatic metalenses, which is essentially attributed to the lower PCE of the composite unit structure (NF1&NF2) at a shorter waveband (around 4 μm). Nevertheless, we emphasize that our approach does not preclude the design of highly efficient metasurfaces, which can be achieved by incorporating other design approaches such as hybrid meta-atoms⁴³ or inverse designs.^{44,45}

In conclusion, we proposed a novel approach for implementing broadband achromatic and polarization-insensitive focusing metadvice in the mid-wavelength infrared range. Different from the state-of-the-art achromatic mechanism, our achromatic designing principle is inspired by the Rayleigh criterion for spot resolution, and the polarization-insensitive merits benefit from the highly integrated layout fashion of two sets of anisotropic nanofins arranged orthogonally or parallel to each other. We validated the design principle by demonstrating polarization-insensitive and achromatically focused metalenses with diffraction-limited focusing behavior while maintaining high focusing efficiency. In particular, the BAPIML with different NAs and sizes are also implemented, robustly confirming the generality of the proposed design approach. In addition, we also demonstrate the versatility of the proposed design method by successfully implementing the generation of the BAPIFOV generator with a constant topological charge. We believe this achromatic and polarization-insensitive method could free one from tedious computing efforts, and the metadvice designed with this method will obtain focusing performance on par with conventional meta-optics involving the mainstream achromatic schemes such as IRM, thereby paving the way for a wide range of potential applications in MWIR.

Acknowledgments

This work was supported by the National Natural Science Foundation of China (Grant No. 12004347), the Scientific and Technological Project in Henan Province (Grant Nos. 222102210063 and 232102320057), the Aeronautical Science Foundation of China (Grant Nos. 2020Z073055002 and 2019ZF055002), the Innovation and Entrepreneurship Training Program for College Students (Grant Nos. 202210485007 and 202210485044), and the Graduate Education Innovation Program Foundation (Grant No. 2022CX53). The authors declare no conflicts of interest.

References

1. S. Wang et al., “A broadband achromatic metalens in the visible,” *Nat. Nanotechnol.* **13**, 227–232 (2018).
2. W. T. Chen et al., “A broadband achromatic metalens for focusing and imaging in the visible,” *Nat. Nanotechnol.* **13**, 220–226 (2018).
3. W. T. Chen et al., “A broadband achromatic polarization-insensitive metalens consisting of anisotropic nanostructures,” *Nat. Commun.* **10**, 355 (2019).
4. M. Khorasaninejad et al., “Metalenses at visible wavelengths: diffraction-limited focusing and subwavelength resolution imaging,” *Science* **352**, 1190–1194 (2016).

5. M. Wang et al., "Varifocal metalens using tunable and ultralow-loss dielectrics," *Adv. Sci.* **10**, 2204899 (2023).
6. H. Yafeng et al., "Spin-multiplexing phase-driven varifocal metalenses for multidimensional beam splitting and binary switching," *Europhys. Lett.* **141**, 55004 (2023).
7. P. Georgi et al., "Optical secret sharing with cascaded metasurface holography," *Sci. Adv.* **7**, eabf9718 (2021).
8. Q. Song et al., "Vectorial metasurface holography," *Appl. Phys. Rev.* **9**, 011311 (2022).
9. I. Javed et al., "Broad-band polarization-insensitive metasurface holography with a single-phase map," *ACS Appl. Mater. Interfaces* **14**, 36019–36026 (2022).
10. R. Zhao, L. Huang, and Y. Wang, "Recent advances in multidimensional metasurfaces holographic technologies," *Photonix* **2**, 1–24 (2020).
11. X. Tian et al., "Broadband generation of polarization-immune cloaking via a hybrid phase-change metasurface," *Photonics* **9**, 56 (2022).
12. X. Tian et al., "Phase-change reconfigurable metasurface for broadband, wide-angle, continuously tunable and switchable cloaking," *Opt. Express* **29**, 5959–5971 (2021).
13. W. Zhu et al., "Polarization-multiplexed silicon metasurfaces for multi-channel visible light modulation," *Adv. Funct. Mater.* **32**, 2200013 (2022).
14. F. Yu et al., "Reconfigurable metasurface with tunable and achromatic beam deflections," *Opt. Mater. Express* **12**, 49–58 (2022).
15. X. Xie et al., "All-metallic geometric metasurfaces for broadband and high-efficiency wavefront manipulation," *Nanophotonics* **9**, 3209–3215 (2019).
16. F. Aieta et al., "Multiwavelength achromatic metasurfaces by dispersive phase compensation," *Science* **347**, 1342–1345 (2015).
17. D. Lin et al., "Photonic multitasking interleaved Si nanoantenna phased array," *Nano Lett.* **16**, 7671–7676 (2016).
18. M. Khorasaninejad et al., "Achromatic metalens over 60 nm bandwidth in the visible and metalens with reverse chromatic dispersion," *Nano Lett.* **17**, 1819–1824 (2017).
19. E. Arbabi et al., "Controlling the sign of chromatic dispersion in diffractive optics with dielectric metasurfaces," *Optica* **4**, 625–632 (2017).
20. S. Wang et al., "Broadband achromatic optical metasurface devices," *Nat. Commun.* **8**, 187 (2017).
21. Q. Cheng et al., "Broadband achromatic metalens in terahertz regime," *Sci. Bull.* **64**, 1525–1531 (2019).
22. H. Zhou et al., "Broadband achromatic metalens in the mid-infrared range," *Phys. Rev. Appl.* **11**, 024066 (2019).
23. M. Liu et al., "Broadband achromatic metalens for linearly polarized light from 450 to 800 nm," *Appl. Opt.* **60**, 9525–9529 (2021).
24. Z.-B. Fan et al., "A broadband achromatic metalens array for integral imaging in the visible," *Light: Sci. Appl.* **8**, 67 (2019).
25. R. J. Lin et al., "Achromatic metalens array for full-colour light-field imaging," *Nat. Nanotechnol.* **14**, 227–231 (2019).
26. H. Zhou et al., "Design of an achromatic optical polarization-insensitive zoom metalens," *Opt. Lett.* **47**, 1263–1266 (2022).
27. P. Sun et al., "Broadband achromatic polarization insensitive metalens over 950 nm bandwidth in the visible and near-infrared," *Chin. Opt. Lett.* **20**, 013601 (2022).
28. Y. Wang et al., "High-efficiency broadband achromatic metalens for near-IR biological imaging window," *Nat. Commun.* **12**, 5560 (2021).
29. J. T. Heiden and M. S. Jang, "Design framework for polarization-insensitive multifunctional achromatic metalenses," *Nanophotonics* **11**, 583–591 (2022).
30. X. Zhang et al., "Broadband polarization-independent achromatic metalenses with unintuitively-designed random-shaped meta-atoms," <https://doi.org/10.48550/arXiv.2103.10845> (2021).
31. T. Zhou et al., "Spin-independent metalens for helicity-multiplexing of converged vortices and cylindrical vector beams," *Opt. Lett.* **45**, 5941–5944 (2020).
32. X. Zang et al., "A multi-foci metalens with polarization-rotated focal points," *Laser Photonics Rev.* **13**, 1900182 (2019).
33. T. Zhou et al., "Helicity multiplexed terahertz multi-foci metalens," *Opt. Lett.* **45**, 463–466 (2020).
34. M. V. Berry, "The adiabatic phase and Pancharatnam's phase for polarized light," *J. Mod. Opt.* **34**, 1401–1407 (1987).
35. S. Pancharatnam and S. Pancharatnam, "Generalized theory of interference, and its applications," *Resonance* **18**, 387–389 (2013).
36. M. Y. Shalaginov et al., "Reconfigurable all-dielectric metalens with diffraction-limited performance," *Nat. Commun.* **12**, 1225 (2021).
37. Y. Zhang et al., "Broadband transparent optical phase change materials for high-performance nonvolatile photonics," *Nat. Commun.* **10**, 4279 (2019).
38. J. Xu et al., "Ge₂Sb₂Se₄Te₁-based multifunctional metalenses for polarization-independent, switchable and dual-mode focusing in the mid-infrared region," *Opt. Express* **29**, 44227–44238 (2021).
39. Y. Liang et al., "High-efficiency, near-diffraction limited, dielectric metasurface lenses based on crystalline titanium dioxide at visible wavelengths," *Nanomaterials* **8**, 288 (2018).
40. A. Arbabi et al., "Dielectric metasurfaces for complete control of phase and polarization with subwavelength spatial resolution and high transmission," *Nat. Nanotechnol.* **10**, 937–943 (2015).
41. M. S. Carstensen et al., "Holographic resonant laser printing of metasurfaces using plasmonic template," *ACS Photonics* **5**, 1665–1670 (2018).
42. H.-H. Hsiao et al., "Integrated resonant unit of metasurfaces for broadband efficiency and phase manipulation," *Adv. Opt. Mater.* **6**, 1800031 (2018).
43. A. Hassanfiroozi et al., "Toroidal-assisted generalized Huygens' sources for highly transmissive plasmonic metasurfaces," *Laser Photonics Rev.* **16**, 2100525 (2022).
44. H. Chung and O. D. Miller, "High-NA achromatic metalenses by inverse design," *Opt. Express* **28**, 6945–6965 (2020).
45. C.-H. Lin et al., "Automatic inverse design of high-performance beam-steering metasurfaces via genetic-type tree optimization," *Nano Lett.* **21**, 4981–4989 (2021).

Ximin Tian received her BS degree in condensed matter physics from Taiyuan University of Technology of China in 2015 and her PhD in optics from the Institute of Physics, Chinese Academy of Sciences in 2018. Now she is an associate professor in Zhengzhou University of Aeronautics. Her research interests cover theory and experiment of metalenses, metasurface cloaks, metasurface holograms, vortex beams, and beyond.

Junwei Xu received her BS degree in condensed matter physics from Taiyuan University of Technology of China in 2015 and worked at SMIC until 2018. Now he is an experimentalist in Zhengzhou University of Aeronautics. His research interests cover theory and experiment of metalenses, metasurface cloaks, vector vortex beams, and beyond.

Zhi-Yuan Li received his BS degree in optoelectronics from the University of Science and Technology of China in 1994 and his PhD in optics from the Institute of Physics, Chinese Academy of Sciences in 1999, where he served as a principal investigator from 2004 to 2016. Now he is a professor in the South China University of Technology. His research interests cover theory and experiment of photonic crystals, nonlinear and ultrafast optics, plasmonics, quantum optics, optical tweezers, nanophotonics, and topological photonics.

Biographies of the other authors are not available.